

# Understanding the Stability of an Unprecedented Si–Be Bond within Quantum Confinement

Asma Harun Maneri, Sailaja Krishnamurty,\* and Krati Joshi\*

Cite This: *ACS Omega* 2023, 8, 14814–14822

Read Online

ACCESS |



Metrics &amp; More

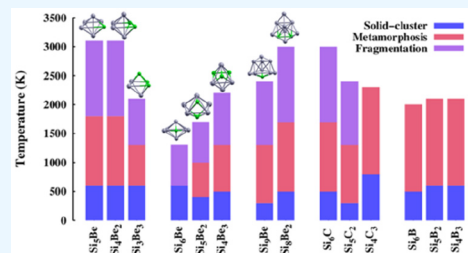


Article Recommendations



Supporting Information

**ABSTRACT:** As of today, the Si–Be bond remains underexplored in the literature, and therefore its anomalous behavior continues to be an unsolved puzzle to date. Therefore, the present study aims at evaluating the integrity of an unprecedented Si–Be bond within quantum confinement. To accomplish this, first-principles-based calculation are performed on Be-doped silicon clusters with atomic sizes 6, 7, and 10. Silicon clusters are sequentially doped with one, two, and three Be atoms, and their thermal response is registered in the temperature range of 200–1500 K, which discloses several research findings. During the course of the simulations, the clusters face various thermal events such as solid cluster phase, rapid structural metamorphosis, and fragmentation. Si–Be nanoalloy clusters are noted to be thermally stable at lower temperatures (200–700 K); however, they begins to disintegrate earlier at a temperature as low as 800 K. This lower stability is attributed to the weak nature of Si and Be heteroatomic interactions, which is corroborated from the structural and electronic property analysis of the doped clusters. In addition to this, the performance of Be-doped clusters at finite temperatures is also compared with the thermal response of two other popular systems, viz., C- and B-doped silicon clusters.



## INTRODUCTION

A century after the concept of chemical bonding was elucidated, some unusual bonds continue to be discovered, causing much excitement and a wide scope for the development of novel materials. In this context, bottom up synthesis methods of nanoclusters have an unparalleled advantage of putting together some of the unprecedented elements for controlled property dependent structure generation with practically no loss of material.<sup>1–3</sup> Several state of the art methods have been deployed to put together monatomic subnanoparticles such as Cu,<sup>4–6</sup> Ga,<sup>7–9</sup> Al,<sup>10</sup> Si,<sup>11–13</sup> Rh,<sup>12–14</sup> Ru,<sup>12,13,15</sup> Fe,<sup>16–19</sup> and V<sup>20</sup> into more mixed binary clusters,<sup>15–17,21–27</sup> resulting in atomic level engineering of property dependent materials.<sup>28–33</sup>

Silicon, being the earth's most abundant element, has not been left behind in this context and has been reported to participate in distinctive or multiple bonding with itself as well as with other heavier elements.<sup>34–36</sup> At the quantum confinement phase space, it has been one of the most widely studied systems both experimentally as well as computationally.<sup>36–54,68,69</sup> While, experimentally, Si has been evidenced to bond with several main group elements such as boron, carbon, nitrogen, oxygen, etc., a bond with the Be atom is one of the most unprecedented ones so far. While its high ionization potentials and small size result in Be forming covalent bonds with many elements, B–Si bonds are quite rare. Beryllium has a tendency to form tetravalent compounds using  $sp^3$  hybrid orbitals to give tetrahedral bonding and forms a polar bond with carbon. Similarly, even a Be–Be bond is an unconventional bond.<sup>58</sup> Experimentally, using both NMR techniques

and single X-ray crystallography, Be–Si bonds have been identified in a series of organometallic compounds.<sup>55,56</sup> In one such report, a combined experimental and theoretical analysis concluded that the  $CpBe(SiMe_3)$  organometallic compound encompasses a polar Be–Si bond.<sup>57</sup> To some extent, beryllium to silicon bonding has been investigated within these compounds; however, the nature of Be–Si bonds within quantum confinement has not been explored.

Taking into consideration the unusual nature of Si–Be bonds, reviewed above, the present investigation focuses on beryllium-doped silicon clusters, viz.,  $Si_5Be$ ,  $Si_6Be$ , and  $Si_9Be$  clusters, where their physicochemical properties have been evaluated using Born–Oppenheimer Molecular Dynamics (BOMD). The finite temperature behavior has been investigated by increasing the concentration of the dopant from 1 to 3. To establish a broader perspective on Be–Si bonds, the thermal behavior of Be-doped clusters is compared with two of the most popular and stable doped silicon systems, i.e., C- and B-doped silicon clusters.

Received: February 20, 2023

Accepted: March 29, 2023

Published: April 12, 2023



## COMPUTATIONAL DETAILS

The structures of the lowest energy conformations of Be-doped silicon clusters ( $\text{Si}_5\text{Be}$ ,  $\text{Si}_6\text{Be}$ , and  $\text{Si}_9\text{Be}$ ) have already been studied extensively in earlier research works.<sup>50</sup> The geometries of the clusters identified in these studies have been obtained and are presented in the Figure 1. The  $\text{Si}_5\text{Be}$ ,  $\text{Si}_6\text{Be}$ , and  $\text{Si}_9\text{Be}$

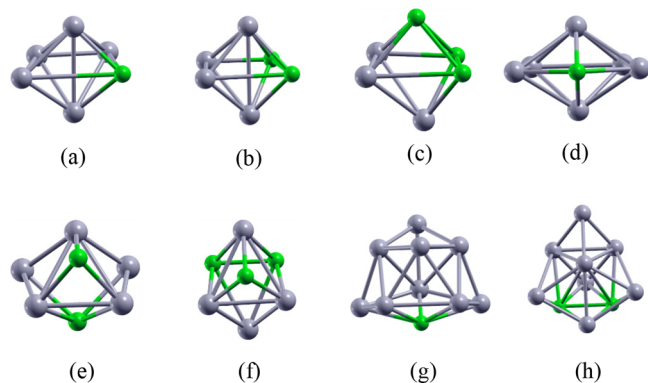


**Figure 1.** Lower energy conformations of (a)  $\text{Si}_5\text{Be}$ , (b)  $\text{Si}_4\text{Be}_2$ , (c)  $\text{Si}_3\text{Be}_3$ , (d)  $\text{Si}_6\text{Be}$ , (e)  $\text{Si}_5\text{Be}_2$ , (f)  $\text{Si}_4\text{Be}_3$ , (g)  $\text{Si}_9\text{Be}$ , and (h)  $\text{Si}_8\text{Be}_2$  clusters. Si atoms are represented in gray color, Be atoms in green color.

clusters are then sequentially doped at various chemically distinct atomic sites with two and three dopant atoms. We believe that the clusters smaller than 6–10 atoms do not represent an ideal case to fully understand the nature of Si–Be bonds via performing BOMD simulations. However, larger clusters (more than 20–30 atoms) would be computationally expensive to perform ab initio molecular dynamics simulations. Therefore, we have selected specific cluster sizes within a range of medium-sized clusters for our investigation. Also, it is noted that the majority of DFT calculations have been focused on these specific cluster sizes within a medium size range. The geometries determined for these clusters ( $\text{Si}_4\text{Be}_2$  and  $\text{Si}_3\text{Be}_3$ ,  $\text{Si}_5\text{Be}_2$  and  $\text{Si}_4\text{Be}_3$ , and  $\text{Si}_8\text{Be}_2$ ) are also displayed in the Figure 1.

All the clusters chosen in the present investigation were optimized using Density Functional Theory (DFT)-based methodology as implemented in deMon 2K code.<sup>59</sup> The optimizations were carried out using Becke exchange with Lee, Yang, and Parr correlation (BLYP) functional<sup>60,61</sup> with the DZVP basis set. No additional polarization functions were added. The GEN-A2 auxiliary functions were set to fit the charge density.<sup>62</sup> The convergence of the geometries was based on gradient and displacement criteria with a threshold value of  $10^{-3}$  au, and criteria for convergence of SCF cycles were set to  $10^{-6}$  au. Only the lowest spin state was considered for all the  $\text{Si}_n\text{X}_m$  ( $X = \text{Be}, \text{B}, \text{and C}$ ,  $n = 6-3, 9-8$ , and  $m = 1-3$ ) clusters in the study. The calculations for each cluster were further extended to evaluate the credibility of the obtained results using a Generalized Gradient Approximation (GGA) functional, viz., a PBE functional,<sup>63</sup> and a meta-GGA, viz., M06 functional.<sup>64</sup>

The lowest energy conformations shown in Figure 1 were subjected to finite temperature simulations using Born–Oppenheimer Molecular Dynamics (BOMD) as implemented in deMon2K for an NVT ensemble. We held the total angular momentum of the cluster to zero, suppressing the cluster rotation. The simulations were carried out between 200 and

1500 K, at temperatures of 200, 300, 400, 500, 600, 700, 800, 900, 1000, 1100, 1300, and 1500 K, respectively. For each temperature, the cluster was equilibrated for a time period of 70 ps followed by a simulation time of 80 ps. The temperature of the cluster was maintained using the Nosé–Hoover thermostat<sup>65,66</sup> as implemented in deMon 2K. The nuclear positions were updated with the velocity Verlet algorithm with a time step of 1 fs. The ionic motions were analyzed and quantified using traditional parameters such as root-mean-squared bond length fluctuations ( $\delta_{\text{rms}}$ ) and the Mean Square Displacements of atoms (MSDs).  $\delta_{\text{rms}}$  is defined as

$$\delta_{\text{rms}} = \frac{2}{N(N-1)} \sum_{i < j} \frac{\sqrt{\langle r_{ij}^2 \rangle_t - \langle r_{ij} \rangle_t^2}}{\langle r_{ij} \rangle_t}$$

where  $N$  is the number of particles in the system,  $r_{ij}$  is the distance between the  $i$ th and  $j$ th particles in the system, and  $\langle \dots \rangle_t$  denotes a time average over the entire trajectory. The MSD of an individual atom is defined as

$$r_i^2(t) \geq \frac{1}{NM} \sum_{m=1}^M \sum_{i=1}^N [R_i(t_{0m} + t) - R_i(t_{0m})]^2$$

where  $N$  is the number of atoms in the system,  $R_i(t_{0m})$  is the instantaneous position of atom  $i$  at  $t_0$ , and  $R_i(t_{0m} + t)$  is the corresponding position of atom  $i$  after a time interval  $t$ . Thus, we average over  $M$  different time origins  $t_{0m}$  spanning the entire trajectory. The interval between the consecutive  $t_{0m}$  for the average was taken to be about 0.0125 ps. The MSD indicates the displacement of atoms in the cluster as a function of time. In the solidlike region, all atoms perform oscillatory motion about fixed positions resulting in a negligible MSD of individual atoms. In a liquidlike state, on the other hand, atoms diffuse throughout the cluster, and the MSD eventually reaches a saturated value of the order of the square of the cluster radius.

## RESULTS AND DISCUSSION

Figure 1 presents the ground state conformers of Be-doped silicon clusters of atomic sizes 6, 7, and 10. The ground state structure of the  $\text{Si}_6$  pristine cluster is a  $D_{4h}$  tetragonal bipyramid as shown in Figure S1a of the Supporting Information (ESI). Doping with a single Be atom results in a slightly deformed tetragonal bipyramid geometry with the Be atom sitting at the corner of the tetragonal ring. Subsequent doping with two and three Be atoms gives rise to ground state geometries where Be atoms acquire an edge and a triangular face of the bipyramid in  $\text{Si}_4\text{Be}_2$  and  $\text{Si}_3\text{Be}_3$  clusters, respectively.

The geometry of the  $\text{Si}_6\text{Be}$  conformer (Figure 1d) is obtained by replacing a silicon atom with a Be atom within the pristine  $\text{Si}_7$  cluster (Figure S1b). The lowest energy conformer is determined to be the one in which the Be atom prefers to stay at the pentagonal ring rather than at the capping site.<sup>50</sup> Followed by this, replacement of another Si atom with a second Be atom is seen to be favorable at the capping position (Figure 1e). In the case of  $\text{Si}_4\text{Be}_3$ , the third Be atom acquires a position at the central four-membered ring of the cluster.

Substitution of a single Si atom with a Be atom within the  $\text{Si}_{10}$  pentagonal prism (Figure S1c) leads to a ground state structure where the Be atom sits at the capping site of the pentagonal ring (Figure 1g). In the case of  $\text{Si}_8\text{Be}_2$ , the two Be atoms acquire an edge of the deformed pyramid (Figure 1h).

**Finite Temperature Behavior.** The finite temperature behavior of  $\text{Si}_n\text{Be}_m$  ( $n = 5-3$ ,  $m = 1-3$ ),  $\text{Si}_n\text{Be}_m$  ( $n = 6-4$ ,  $m = 1-3$ ), and  $\text{Si}_n\text{Be}_m$  ( $n = 9-8$ ,  $m = 1-2$ ) clusters is discussed here. Throughout the course of their trajectories, the clusters are seen to undergo some major thermal events such as solid cluster phase (starting geometry remains intact), structural transformation (transition into different high energy conformations), and fragmentation (disintegration into specific fragments). The temperature range for which these events last varies with the cluster. The course of actions picked up by these clusters at finite temperature is discussed in detail in the following sections.

$\text{Si}_n\text{Be}_m$  ( $n = 5-3$ ,  $m = 1-3$ ). We analyze the ionic motion of beryllium-doped silicon clusters as noted in the simulation trajectories. The  $\text{Si}_3\text{Be}$  cluster is seen to remain in its original conformation until 600 K (Figure 2). Around 700 K and

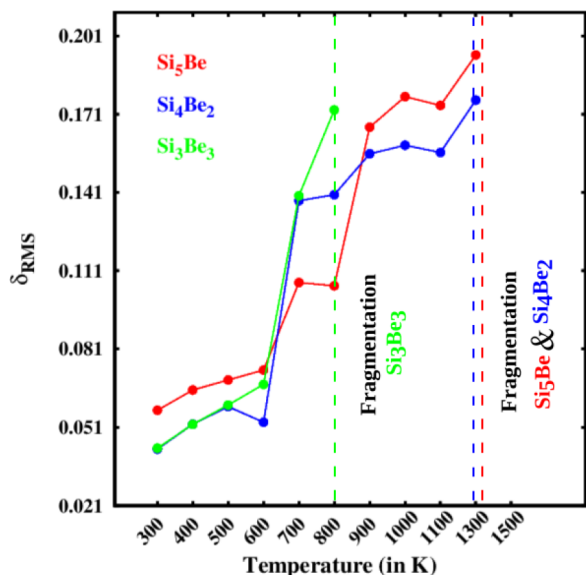


**Figure 2.**  $\delta_{\text{rms}}$  plots for  $\text{Si}_5\text{Be}$ ,  $\text{Si}_4\text{Be}_2$ , and  $\text{Si}_3\text{Be}_3$  at various temperatures.

onward, the cluster experiences rigorous structural transitions giving rise to different conformers. Some of the notable conformers are presented in Figure S5a–c (Supporting Information). The rate of atomic displacements increases, which eventually leads to the Be atom transiting away from the cluster above 1300 K. This can be noticed in the MSD plots shown in Figure S2a.  $\text{Si}_4\text{Be}_2$  behaves similarly to  $\text{Si}_5\text{Be}$ , viz., the cluster undergoes conformational transitions from 700 K followed by its fragmentation above 1300 K (Figure S5d–g). During the structural transition phase, the two Be atoms translate away from the central ring of the cluster, giving rise to a conformation where the  $\text{Si}_4$  acquires a bent rhomboid shape (Figure S5d–g). Eventually, above 1300 K the  $\text{Be}_2$  dimer exits the cluster, leaving behind a planar  $\text{Si}_4$  cluster.

The thermal response recorded for the  $\text{Si}_3\text{Be}_3$  cluster is the same as that for  $\text{Si}_5\text{Be}$  and  $\text{Si}_4\text{Be}_2$  clusters until 600 K. As the temperature increases to 700 K, two of the beryllium atoms transit to one plane while the other beryllium atom moves in another plane as a consequence of constant metamorphosis. In contrast to the other two six-atom clusters ( $\text{Si}_5\text{Be}$  and  $\text{Si}_4\text{Be}_2$ ),  $\text{Si}_3\text{Be}_3$  with an equal concentration of Si and Be fragments into  $\text{Si}_3$  and  $\text{Be}_3$  (Figure S5h–k) at a much earlier temperature (800 K), indicating lower thermal stability.

Altogether, the solid cluster phase (starting structure is retained) of  $\text{Si}_n\text{Be}_m$  ( $n = 5-3$ ,  $m = 1-3$ ) clusters continue until 500–600 K, accompanied by rigorous structural transitions and comparatively sooner disintegration of the clusters at finite temperature.

$\text{Si}_n\text{Be}_m$  ( $n = 6-4$ ,  $m = 1-3$ ). The bond length fluctuations of  $\text{Si}_6\text{Be}$  are measured as a function of temperature and are plotted in Figure 3. The  $\delta_{\text{rms}}$  values (red curve) vary marginally

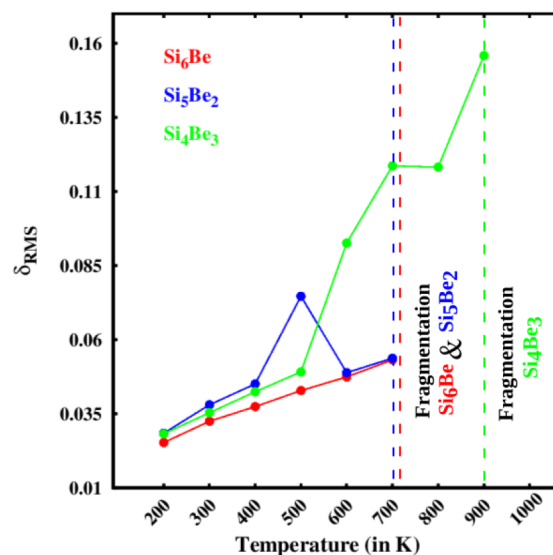


**Figure 3.**  $\delta_{\text{rms}}$  plots for  $\text{Si}_6\text{Be}$ ,  $\text{Si}_5\text{Be}_2$ , and  $\text{Si}_4\text{Be}_3$  at various temperatures.

from 0.03 to 0.05. Thus, the only movement noted in this temperature range is that the atoms in the cluster vibrate about their original positions until 700 K. The Be atom sitting at the center of the pentagonal ring begins to deviate from its equilibrium position giving rise to a distorted pentagonal bipyramidal conformation (Figure S6). Following this, the six Si atoms form a square-pyramidal structure with a Si capping and a Be atom forming a dangling bond with a Si atom above 800 K (Figure S6a–c). Beyond this temperature, the Be atom transits away from the silicon cluster leading into its dissociation into  $\text{Si}_6$  and Be.

This is quantified through the analysis of the mean square displacements given in Figure S3 of the ESI. Figure S3a and b indicates that the atomic displacements are negligible at 200 K and minimal at 600 K, whereas they increase to a maximum value at 800 K, indicative of Be dissociation (represented by gray lines) from the rest of the silicon cluster as demonstrated by the geometries (snapshots from the trajectories) shown in the Figure S6.

In the case of  $\text{Si}_5\text{Be}_2$ , it is noted that the cluster undergoes fragmentation at the same temperature (around 800 K) as the  $\text{Si}_6\text{Be}$  cluster. The two Be atoms dissociate from  $\text{Si}_5$ , which can be corroborated from the  $\delta_{\text{rms}}$  plots presented in Figure 3. Besides this, a hump is noted at 500 K in the  $\delta_{\text{rms}}$  curve on account of the emergence of another conformation as shown in Figure S6e of the ESI. The cluster remains in this conformation at 600 and 700 K as well, where  $\text{Si}_3$  forms a capped tetrahedron with two Be atoms acquiring two apex positions within the cluster. Above this temperature, the two Be atoms form a dimer and leave the cluster as shown in Figure S6f and g of the ESI. Similar behavior is also noted from the mean-square



displacement of atoms given in Figure S3b at 200, 500, and 800 K, respectively. The major difference in the thermal response of the  $\text{Si}_3\text{Be}_2$  and  $\text{Si}_6\text{Be}$  clusters is that the former retains its initial structure until its fragmentation while the later experiences structural transformation before disintegrating into  $\text{Be}_2$  and  $\text{Si}_5$  fragments.

From 200 to 500 K,  $\text{Si}_4\text{Be}_3$  encounters a solid cluster phase. As noted from the  $\delta_{\text{rms}}$  plots given in Figure 3, the cluster is seen to fragment only above 900 K. Before undergoing fragmentation, the  $\text{Si}_4\text{Be}_3$  cluster faces structural transformations from 600 to 800 K (Figure S7a–d). The conformational changes and the subsequent dissociation of Be atoms one after the other from the silicon matrix are also assessed through the mean-square atomic displacement given in Figure S3c at 200, 600, and 1000 K, respectively.

Overall, the thermal response of 7-atom beryllium-doped silicon clusters is similar to that of  $\text{Si}_n\text{Be}_m$  ( $n = 5-3$ ,  $m = 1-3$ ) clusters in the lower temperature range ( $<700$  K, solid cluster phase). However, in the former case, the cluster experiences premature disintegration (700–900 K), and in the latter case the fragmentation is noticed at higher temperatures (at 1300 K, except  $\text{Si}_3\text{Be}_3$ ).

$\text{Si}_n\text{Be}_m$  ( $n = 9-8$ ,  $m = 1-2$ ). In order to establish a better understanding, thermal behavior of the  $\text{Si}_n\text{Be}_m$  cluster with higher atomic size (10 atoms) is also taken into account. In this case, doping is restricted at two atoms only, since increasing the concentration of beryllium atoms to 3 leads to isoenergetic structures.

Different conformers of the  $\text{Si}_9\text{Be}$  cluster begin to emerge in the simulation trajectories at higher temperature after preserving its initial structure until 400 K as displayed by the  $\delta_{\text{rms}}$  plots in Figure 4. In the course of structural transition

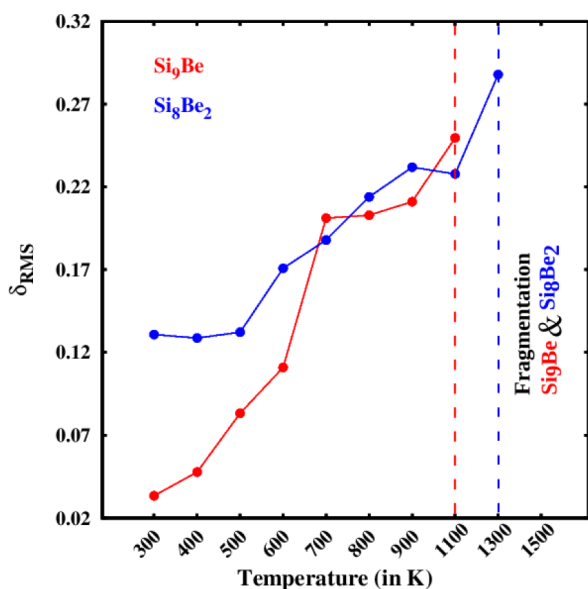


Figure 4.  $\delta_{\text{rms}}$  plots as a function of temperature for  $\text{Si}_9\text{Be}$ , and  $\text{Si}_8\text{Be}_2$  clusters.

(between 400 and 1100 K), the cluster gives rise to a pyramidal cage conformation as shown in Figure S7b. Afterward, the single beryllium atom eventually shifts away from the remaining cluster above 1100 K. Contrastingly, the  $\text{Si}_8\text{Be}_2$  cluster retains its starting conformer until 500 K, followed by a conformational transformation (Figure S7d–f)

at 600 K which subsequently leads to its fragmentation at 1300 K, corroborated from the MSD plots (Figure S4b).

As compared to  $\text{Si}_n\text{Be}_m$  ( $n = 9-8$ ,  $m = 1-2$ ) clusters, the duration of the solid cluster phase (200–500 K) is comparatively longer in the case of smaller sized Be-doped silicon clusters (200–700 K). In general, among the Be-doped silicon clusters, it is eminent that all the systems are vulnerable at high temperature, and they undergo fragmentation. The lowest and highest temperatures at which these clusters disintegrate are 700 K ( $\text{Si}_6\text{Be}$  and  $\text{Si}_3\text{Be}_2$ ) and 1300 K ( $\text{Si}_3\text{Be}$ ,  $\text{Si}_4\text{Be}_2$ , and  $\text{Si}_8\text{Be}_2$ ), respectively. These doped clusters breaking at earlier temperatures indicates lower structural strength which ultimately amounts to the nature of interaction between the dopant and the host cluster (Si–Be).

*Case Study: Comparison with  $\text{Si}_n\text{C}_m$  and  $\text{Si}_n\text{B}_m$  ( $n = 6-4$ ,  $m = 1-3$ ).* In the next set of case studies, we performed a molecular dynamics study on two of the most notable and stable doped silicon clusters, viz.,  $\text{Si}_n\text{C}_m$  and  $\text{Si}_n\text{B}_m$  ( $n = 6-4$ ,  $m = 1-3$ ). The physicochemical properties of these clusters have been studied significantly in the literature.<sup>46,48–50</sup> The ground state geometries of these clusters are presented in Figure S8 of the ESI. Similar to the case of Be doping, the concentration of the dopant is varied from 1 to 3 in these cases as well.

After preserving their respective initial geometries until 500 and 400 K,  $\text{Si}_6\text{C}$  and  $\text{Si}_5\text{C}_2$  clusters experience rapid structural transformations until high temperatures (1300 and 1100 K, respectively). Above these temperatures, the single- and double-carbon-doped silicon clusters disintegrate into (Si–C–Si +  $\text{Si}_3$ ) and (Si–C–Si and  $\text{Si}_3\text{C}$ ) fragments. This dynamical behavior at defined temperatures is corroborated from their  $\delta_{\text{rms}}$  plots presented in Figure 5.

In the case of the  $\text{Si}_4\text{C}_3$  cluster, the ground state conformer is noted until 800 K, and from 900 K onward the  $\text{Si}_4\text{C}_3$  cluster experiences conformational transitions. The stability behavior and fragmentation pattern in carbon-doped silicon clusters are further elaborated upon in terms of mean-square displacements, Figure S9 of the ESI. For C-doped silicon clusters, lower and medium concentrations of the dopant result in earlier disintegration of  $\text{Si}_6\text{C}$  and  $\text{Si}_5\text{C}_2$  clusters. Contrastingly,  $\text{Si}_4\text{C}_3$  with a higher dopant concentration remains unbroken until very high temperatures.

The root-mean-square bond length fluctuations of sequentially doped  $\text{Si}_6\text{B}$ ,  $\text{Si}_3\text{B}_2$ , and  $\text{Si}_4\text{B}_3$  clusters are presented in Figure S9. Minimal  $\delta_{\text{rms}}$  values are noted around 500 and 600 K, viz., 0.05, 0.043, and 0.045 for  $\text{Si}_6\text{B}$ ,  $\text{Si}_3\text{B}_2$ , and  $\text{Si}_4\text{B}_3$  clusters, respectively, revealing that the clusters vibrate around their original positions. Beyond these temperatures, their trajectories showcase rapid structural metamorphosis. However, their geometries remain unfragmented throughout the course of the simulations even at higher temperature (Figure S10 of the ESI).

In general, among the three different types of doped silicon clusters, sequential doping with Be results in earlier disintegration of the clusters at temperatures as low as 700 K. On the other hand, C- and B-doped clusters perform well at higher temperatures. In the former case, fragmentation is witnessed at high temperatures (1300 K), while in the latter case, the clusters remain unbroken during the course of simulations. These behavior patterns are the direct manifestation of the dopant-to-cluster interactions, viz., Si–Be, Si–C, and Si–B. The dominance of these interactions is also evident in the fragmentation channels of the respective doped clusters (Figure S12). For instance, the predominant fragments noticed

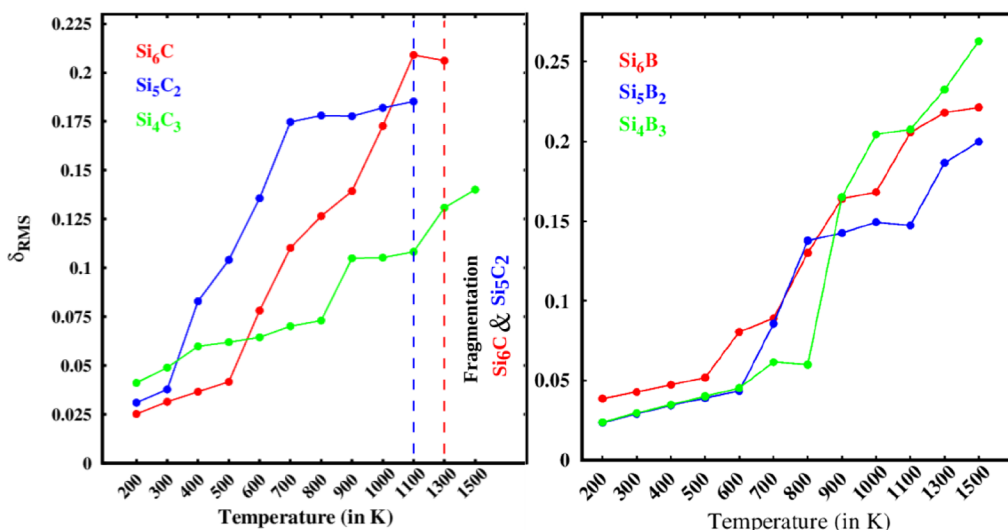


**Figure 5.** Root-mean-square bond length fluctuations ( $\delta_{rms}$ ) for 7-atom C-doped silicon clusters ( $\text{Si}_6\text{C}$ ,  $\text{Si}_5\text{C}_2$ , and  $\text{Si}_4\text{C}_3$ ) and B-doped ( $\text{Si}_6\text{B}$ ,  $\text{Si}_5\text{B}_2$ , and  $\text{Si}_4\text{B}_3$ ) silicon clusters.

for C-doped clusters are ( $\text{Si}-\text{C}-\text{Si} + \text{Si}_3$ ), ( $\text{Si}-\text{C}-\text{Si} + \text{Si}_3\text{C}$ ), and ( $\text{Si}-\text{C}-\text{Si} + \text{Si}_2\text{C}_2$ ). On the other hand,  $\text{Si}_n\text{Be}_m$  nanoalloy clusters disintegrate into their respective constituent particles, viz.,  $\text{Si}_n + \text{Be}_m$ . This again highlights that A–A and B–B interactions are much more dominant than A–B interaction within  $\text{Si}_n\text{Be}_m$  nanoalloy clusters.

Overall, Be-doped silicon clusters are stable around room temperature (300–700 K). The Si–Be bond is strong enough to hold the ground state structure intact (solid cluster phase) at lower temperatures. However, it is not as strong as Si–C or Si–B bonds, and therefore the clusters undergo rapid fragmentation at finite temperatures. The relative duration of each phase, viz, solid–cluster, metamorphosis, and fragmentation, for all the nanoalloy clusters is presented in Figure 6.

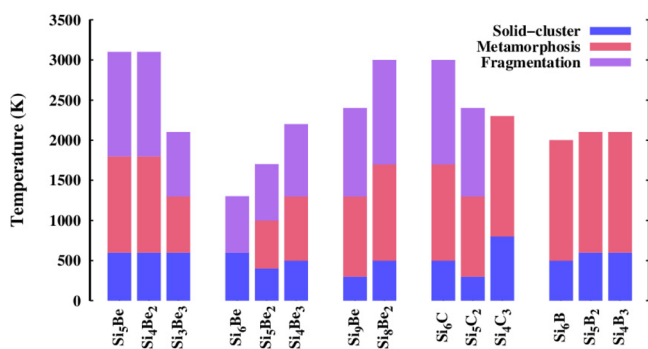


**Figure 6.** Duration of the three phases for Be-, C-, and B-doped clusters considered in the study.

**Si–Be vs Si–B vs Si–C.** To discern the underlying factors responsible for the earlier disintegration of Be-doped silicon clusters, their structural and electronic properties are compared with those of boron- and carbon-doped silicon clusters (7-atom size). Si–Be bonds are one of the scarcely discussed bonds in chemistry. While the strength of the Si–Si bond is reported to be around  $327 \pm 10.0$  kJ/mol, and Be–Be bond energy is reported to be around 59 kJ/mol, there is no practical information on the Si–Be bond energy.<sup>67</sup> The most fundamental structural variation noted as a function of sequential Be doping is a marginal enlargement of Si–Si

interatomic bond distances. The average Si–Si bond distance within the  $\text{Si}_7$  cluster is 2.54 Å, which increases to 2.58, 2.57, and 2.62 Å in the case of  $\text{Si}_6\text{Be}$ ,  $\text{Si}_5\text{Be}_2$ , and  $\text{Si}_4\text{Be}_3$  clusters, respectively. The Si–Be, Si–B, and Si–C interatomic bond distances are compared and plotted in Figure 7. The figure

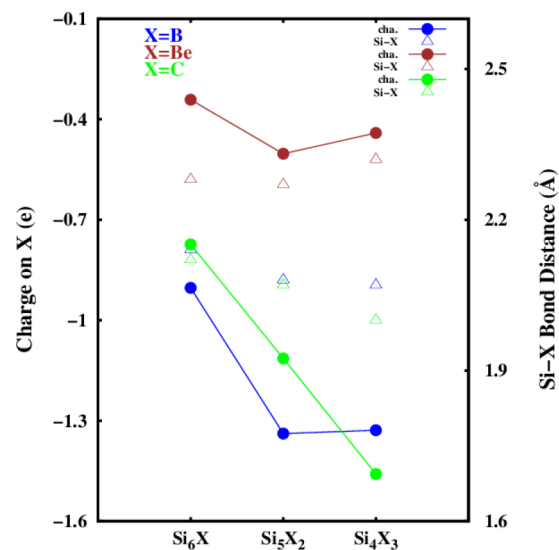


**Figure 7.** Löwdin atomic charges (B, Be, and C) and Si–X interatomic bond distances for  $\text{Si}_6\text{X}$ ,  $\text{Si}_5\text{X}_2$ , and  $\text{Si}_4\text{X}_3$  clusters (X = B, Be, and C).

clearly indicates that Be doping results in lengthening of Si–Be bonds (2.27–2.32 Å) as compared to Si–C and Si–B bonds, where the average bond distance value ranges between 2.01 and 2.14 Å. This trend in the bond length values validates that dopant-to-cluster interactions are comparatively weak in the case of  $\text{Si}_n\text{Be}_m$  clusters as compared to carbon- and boron-doped clusters.

To substantiate this further, Löwdin atomic charge distributions and Frontier Molecular Orbitals (FMOs) are plotted for these clusters (X = Be, B, and C) in Figures 7 and 8. It is noticed that Be atoms are able to gain only a minute amount of charge (–0.34 to –0.5 e) from the rest of the silicon

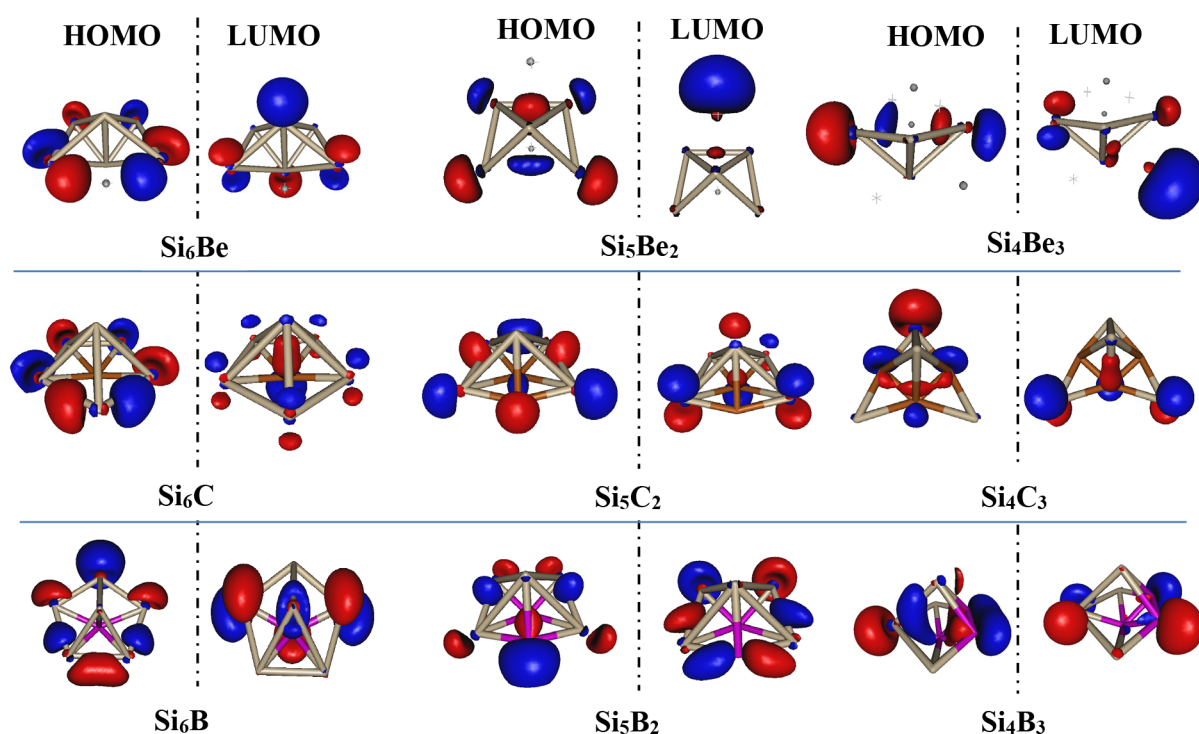


**Figure 8.** Frontier molecular orbitals (FMOs) of Be-, C-, and B-doped silicon clusters of atomic size 7.

cluster. In contrast to this, carbon and boron atoms retain a quantum amount of charge ranging between  $-0.7$  and  $-1.5$  e within  $\text{Si}_n\text{C}_m$  and  $\text{Si}_n\text{B}_m$  clusters, respectively. The charge transfer occurring between the silicon cluster and the dopant atoms is also reflected by their corresponding molecular orbitals (Figure 8). The HOMOs and LUMOs of  $\text{Si}_n\text{C}_m$  and  $\text{Si}_n\text{B}_m$  clusters represent substantial overlapping between the atomic orbitals of silicon atoms and B/C atoms. Additionally, there is a significant contribution from the silicon atoms to the molecular orbital density. However, no such overlapping is noticed between atomic orbitals of the dopant and silicon atoms for  $\text{Si}_n\text{Be}_m$  clusters. Also, the participation of silicon atoms in the formation of molecular orbitals is either very feeble or missing. These characteristics reflected by the FMOs reiterate that Si to Be interactions are relatively weak, resulting in longer Si–Be bonds and low charge transfer between Si and Be atoms. Consequently, as compared to  $\text{Si}_n\text{C}_m$  and  $\text{Si}_n\text{B}_m$  clusters, Be doping leads to fragile clusters, and therefore they undergo fragmentation at earlier temperatures.

## CONCLUSIONS

In the present investigation BOMD simulations are performed on Be-doped silicon clusters with atomic sizes 6, 7, and 10. In order to understand the anomalous nature of Si–Be bonds, a comparison of thermal response between Be-, C-, and B-doped silicon clusters is also conducted. The salient outcomes of the investigation are as follows.

- Be-doped silicon clusters experience various thermal events during the course of simulations, such as solid cluster phase, rapid structural metamorphosis, and fragmentation. The solid cluster phase lasts longer for smaller Si–Be clusters as compared to larger sized clusters ( $\text{Si}_9\text{Be}$ ).
- The clusters tend to disintegrate earlier at temperatures as low as 700–900 K ( $\text{Si}_6\text{Be}$ ,  $\text{Si}_5\text{Be}_2$ , and  $\text{Si}_4\text{Be}_3$ ) and as

high as 1300 K ( $\text{Si}_5\text{Be}$ ,  $\text{Si}_4\text{Be}_2$ , and  $\text{Si}_3\text{Be}_3$ ) respectively. This behavior is indicative of the comparatively weak nature of the interaction between the dopant and the host cluster (Si–Be).

- The thermal response of Be-doped clusters contradicts that of C- and B-doped clusters. In the former case (C), the clusters disintegrate only at high temperatures (around 1300 K), while in the latter case (B), the clusters remain unfragmented throughout the simulations at finite temperature.
- Si–Be nanoalloy clusters are stable at room temperature. The Si–Be bond is strong enough to hold the ground state structure intact (solid cluster phase) at lower temperatures. However, it is not as strong as Si–C or Si–B bonds, and therefore it undergoes rapid fragmentation at finite temperatures.
- Structural and electronic property analysis, viz., atomic charges and frontier molecular orbitals: Minimal overlapping between Be and Si atomic orbitals leads to lower charge transfer which in turn results in lengthening of Be–Si bonds and thereby causes the clusters to break soon at earlier temperatures (700 K).

Although Si–Be based systems have not been understood well, the current study clearly concludes that within quantum confinements, the Si–Be nanoalloy clusters are thermally stable at lower temperatures (room temperature). However, at higher temperatures they are quite vulnerable owing to the poor heteroatomic (Si–Be) interactions, and therefore they undergo fragmentation.

## ASSOCIATED CONTENT

### Supporting Information

The Supporting Information is available free of charge at <https://pubs.acs.org/doi/10.1021/acsomega.3c01133>.



Ground state structures of pristine silicon clusters, mean-squared displacements (MSDs) at finite temperature, snapshots of conformers noted in the simulation trajectories, tabulated geometrical parameters, and Cartesian coordinates of the clusters considered in the present investigation (PDF)

## AUTHOR INFORMATION

### Corresponding Authors

**Sailaja Krishnamurthy** – Physical and Materials Chemistry Division, CSIR-National Chemical Laboratory (CSIR-NCL), Pune 411008, India; Academy of Scientific and Innovative Research (AcSIR), Gaziabad 201002, India; [orcid.org/0000-0001-5090-1892](https://orcid.org/0000-0001-5090-1892); Email: [k.sailaja@ncl.res.in](mailto:k.sailaja@ncl.res.in), [sailaja.raaj@gmail.com](mailto:sailaja.raaj@gmail.com)

**Krati Joshi** – Physical and Materials Chemistry Division, CSIR-National Chemical Laboratory (CSIR-NCL), Pune 411008, India; [orcid.org/0000-0002-8692-9835](https://orcid.org/0000-0002-8692-9835); Email: [krati.joshi81@gmail.com](mailto:krati.joshi81@gmail.com), [kp.joshi@ncl.res.in](mailto:kp.joshi@ncl.res.in)

### Author

**Asma Harun Maneri** – Physical and Materials Chemistry Division, CSIR-National Chemical Laboratory (CSIR-NCL), Pune 411008, India; Academy of Scientific and Innovative Research (AcSIR), Gaziabad 201002, India

Complete contact information is available at:  
<https://pubs.acs.org/10.1021/acsomega.3c01133>

### Notes

The authors declare no competing financial interest.

## ACKNOWLEDGMENTS

K.J. and S.K. acknowledge the CSIR-centre of scientific and industrial research, India, for providing financial support (HCP044-08) throughout the research works. A.H.M. acknowledges the University Grants Commission (UGC), India, for providing a Senior Research Fellowship (SRF). The authors also acknowledge high performance computing facilities at CSIR-National Chemical Laboratory (CSIR-NCL, Pune) and PARAM Brahma facility under the National Supercomputing Mission, Government of India at Indian Institute of Science, Education and Research (IISER), Pune, India.

## REFERENCES

- (1) Zhu, L.; Gharib, M.; Becker, C.; Zeng, Y.; Ziefuß, A. R.; Chen, L.; Alkilany, A. M.; Rehbock, C.; Barcikowski, S.; Parak, W. J.; Chakraborty, I. Synthesis of Fluorescent Silver Nanoclusters: Introducing Bottom-Up and Top-Down Approaches to Nanotechnology in a Single Laboratory Class. *J. Chem. Educ.* **2020**, *97*, 239–243.
- (2) de Oliveira, P. F. M.; Torresi, R. M.; Emmerling, F.; Camargo, P. H. C. Challenges and opportunities in the bottom-up mechanochemical synthesis of noble metal nanoparticles. *J. Mater. Chem. A* **2020**, *8*, 16114–16141.
- (3) Bain, D.; Maity, S.; Patra, A. Opportunities and challenges in energy and electron transfer of nanocluster based hybrid materials and their sensing applications. *Phys. Chem. Chem. Phys.* **2019**, *21*, 5863–5881.
- (4) Lin, Y.-S.; Lin, Y.-F.; Nain, A.; Huang, Y.-F.; Chang, H. T. A critical review of copper nanoclusters for monitoring of water quality. *Sensors and Actuators Reports*. **2021**, *3*, 100026.
- (5) Yan, W.; Zhang, J.; Abbas, M.; Li, Y.; Hussain, S. Z.; Mumtaz, S.; Song, Z.; Hussain, I.; Tan, B. Facile synthesis of ultrastable fluorescent

copper nanoclusters and their cellular imaging application. *Nanomaterials* **2020**, *10*, 1678.

(6) Hu, X.; Liu, T.; Zhuang, Y.; Wang, W.; Li, Y.; Fan, W.; Huang, Y. Recent advances in the analytical applications of copper nanoclusters. *TrAC Trends in Anal. Chem.* **2016**, *77*, 66–75.

(7) Lertanantawong, B.; Riches, J. D.; O'Mullane, A. P. Room Temperature Electrochemical Synthesis of Crystalline GaOOH Nanoparticles from Expanding Liquid Metals. *Langmuir*. **2018**, *34*, 7604–7611.

(8) Nucciarelli, F.; Bravo, I.; Catalan-Gomez, S.; Vázquez, L.; Lorenzo, E.; Pau, J. L. High ultraviolet absorption in colloidal gallium nanoparticles prepared from thermal evaporation. *Nanomaterials*. **2017**, *7*, 172.

(9) Knight, M. W.; Coenen, T.; Yang, Y.; Brenny, B. J. M.; Losurdo, M.; Brown, A. S.; Everitt, H. O.; Polman, A. Gallium plasmonics: Deep subwavelength spectroscopic imaging of single and interacting gallium nanoparticles. *ACS Nano* **2015**, *9*, 2049–2060.

(10) Wu, H.; Cheng, X.; Dong, H.; Xie, S.; He, S. Aluminum nanocrystals evolving from cluster to metallic state: Size tunability and spectral evidence. *Nano Res.* **2022**, *15*, 838–844.

(11) Farirai, F.; Ozonoh, M.; Anikete, T. C.; Eterigho-Ikelegbe, O.; Mupa, M.; Zeyi, B.; Daramola, M. O. Methods of extracting silica and silicon from agricultural waste ashes and application of the produced silicon in solar cells: a mini-review. *Int. J. Sustain. Eng.* **2021**, *14*, 57–78.

(12) Elangovan, H.; Sengupta, S.; Narayanan, R.; Chattopadhyay, K. Silicon nanoparticles with UV range photoluminescence synthesized through cryomilling induced phase transformation and etching. *J. Mater. Sci.* **2021**, *56*, 1515–1526.

(13) Jeong, Y. K.; Huang, W.; Vilá, R. A.; Huang, W.; Wang, J.; Kim, S. C.; Kim, Y. S.; Zhao, J.; Cui, Y. Microclusters of Kinked Silicon Nanowires Synthesized by a Recyclable Iodide Process for High-Performance Lithium-Ion Battery Anodes. *Adv. Energy Mater.* **2020**, *10*, 2002108.

(14) Cheng, W.; Peng, Y.; Wang, Y.; Jiang, W.; Long, Y.; Fan, G. Amino-group and space-confinement assisted synthesis of small and well-defined Rh nanoparticles as efficient catalysts toward ammonia borane hydrolysis. *Int. J. Hydrogen Energy*. **2021**, *46*, 2204–2212.

(15) Pang, B.; Ma, Y.; Tian, Z.; Liu, J.; Wu, S.; Teng, D.; Li, P.; Liang, C. Solvents-dependent selective fabrication of face-centered cubic and hexagonal close-packed structured ruthenium nanoparticles during liquid-phase laser ablation. *J. Colloid Interface Sci.* **2021**, *585*, 452–458.

(16) Yang, J.; Hu, J.; Weng, M.; Tan, R.; Tian, L.; Yang, J.; Amine, J.; Zheng, J.; Chen, H.; Pan, F. Fe-Cluster Pushing Electrons to N-Doped Graphitic Layers with Fe<sub>3</sub>C(Fe) Hybrid Nanostructure to Enhance O<sub>2</sub> Reduction Catalysis of Zn-Air Batteries. *ACS Appl. Mater. Interfaces*. **2017**, *9*, 4587–4596.

(17) Jimenez, R. E.; Bunce, N. J.; Peng, Z.; Wang, Y.; Gupta, R. K.; Kama, S. P. Mixed protein templated iron-nanoclusters exhibit photoluminescence in the visible and near-infrared region. *2017 IEEE 17th International Conference on Nanotechnology (IEEE-NANO)*, 2017; pp 78–82.

(18) Fu, N.; Wei, H.-M.; Lin, H.-L.; Li, L.; Ji, C.-H.; Yu, N.-B.; Chen, H.-J.; Han, S.; Xiao, G.-Y. Iron Nanoclusters as Template/Activator for the Synthesis of Nitrogen Doped Porous Carbon and Its CO<sub>2</sub> Adsorption Application. *ACS Appl. Mater. Interfaces*. **2017**, *9*, 9955–9963.

(19) Ebrahiminezhad, A.; Taghizadeh, S.; Ghasemi, Y.; Berenjian, A. Green synthesized nanoclusters of ultra-small zero valent iron nanoparticles as a novel dye removing material. *Sci. Total Environ.* **2018**, *621*, 1527–1532.

(20) Zhang, H.; Cui, C.; Yan, M.; Geng, L.; Wu, H.; Jia, Y.; Luo, Z.; Li, S. D. An oxygen-passivated vanadium cluster [V@V<sub>10</sub>O<sub>15</sub>]<sup>-</sup> with metal-metal coordination produced by reacting V<sub>n</sub><sup>-</sup> with O<sub>2</sub>. *Phys. Chem. Chem. Phys.* **2021**, *23*, 921–927.

(21) Yang, B.; Xu, J.; Bin, D.; Wang, J.; Zhao, J.; Liu, Y.; Li, B.; Fang, X.; Liu, Y.; Qiao, L.; Liu, L.; Liu, B.; et al. Amorphous phosphatized ruthenium-iron bimetallic nanoclusters with Pt-like activity for

- hydrogen evolution reaction. *Appl. Catal. B: Environ.* **2021**, *283*, 119583.
- (22) Ramos, R. M. C. R.; Regulacio, M. D. Controllable Synthesis of Bimetallic Nanostructures Using Biogenic Reagents: A Green Perspective. *ACS Omega*. **2021**, *6*, 7212–7228.
- (23) Rajeev, R.; Datta, R.; Varghese, A.; Sudhakar, Y. N.; George, L. Recent advances in bimetallic based nanostructures: Synthesis and electrochemical sensing applications. *Microchem. J.* **2021**, *163*, 105910.
- (24) Szumelda, T.; Drelinkiewicz, A.; Kosydar, R.; Gurgul, J.; Duraczynska, D. Synthesis of carbon-supported bimetallic palladium-iridium catalysts by microemulsion: characterization and electrocatalytic properties. *J. Mater. Sci.* **2021**, *56*, 392–414.
- (25) Yang, Y.; Ashraf, M. A.; Fakhri, A.; Gupta, V. K.; Zhang, D. Facile synthesis of gold-silver/copper sulfide nanoparticles for the selective/sensitive detection of chromium, photochemical and bactericidal application. *Spectrochim. Acta Part A: Mol. and Biomol. Spectrosc.* **2021**, *249*, 119324.
- (26) Guadagnini, A.; Agnoli, S.; Badocco, D.; Pastore, P.; Coral, D.; van Raap, M. B. F.; Forrer, D.; Amendola, V. Facile synthesis by laser ablation in liquid of nonequilibrium cobalt-silver nanoparticles with magnetic and plasmonic properties. *J. Colloid Interface Sci.* **2021**, *585*, 267–275.
- (27) Angaru, G. K. R.; Choi, Y. L.; Lingamdinne, L. P.; Choi, J. S.; Kim, D. S.; Koduru, J. R.; Yang, J. K.; Chang, Y. Y. Facile synthesis of economical feasible fly ash-based zeolite-supported nano zerovalent iron and nickel bimetallic composite for the potential removal of heavy metals from industrial effluents. *Chemosphere*. **2021**, *267*, 128889.
- (28) El-Mansy, M. A. M.; Osman, W.; Abdelsalam, H. The electronic and optical absorption properties of pristine, homo and hetero Bi-nanoclusters. *Chem. Phys.* **2021**, *544*, 111113.
- (29) Hua, Y.; Liu, Y.; Jiang, G.; Du, J.; Chen, J. Geometric transition and electronic properties of titanium-doped aluminum clusters:  $Al_nTi$  ( $n = 2–24$ ). *J. Phys. Chem. A* **2013**, *117*, 2590–2597.
- (30) Tsiotsias, A. I.; Charisiou, N. D.; Yentekakis, I. V.; Goula, M. A. Bimetallic Ni-based catalysts for  $CO_2$  methanation: A review. *Nanomaterials*. **2021**, *11*, 28.
- (31) Chen, X.; Zhao, J.-X.; Wang, J.-W.; Liu, Y.; Wang, L.-C.; Weerasooriya, R.; Wu, Y.-C. Doping ZIF-67 with transition metals results in bimetallic centers for electrochemical detection of Hg(II). *Electrochim. Acta* **2021**, *387*, 138539.
- (32) Kaur, A.; Kaur, G.; Singh, P. P.; Kaushal, S. Supported bimetallic nanoparticles as anode catalysts for direct methanol fuel cells: A review. *Int. J. Hydrogen Energy*. **2021**, *46*, 15820–15849.
- (33) Gregory, S. A.; Hanus, R.; Atassi, A.; Rinehart, J. M.; Wooding, J. P.; Menon, A. K.; Losego, M. D.; Snyder, G. J.; Yee, S. K. Quantifying charge carrier localization in chemically doped semiconducting polymers. *Nat. Mater.* **2021**, *20*, 1414–1421.
- (34) Agarwal, A.; Bose, S. K. Bonding Relationship between Silicon and Germanium with Group 13 and Heavier Elements of Groups 14–16. *Chemistry An Asian J.* **2020**, *15*, 3784–3806.
- (35) Nukazawa, T.; Iwamoto, T. An Isolable Tetrasilicon Analogue of a Planar Bicyclo[1.1.0]butane with  $\pi$ -Type Single-Bonding Character. *J. Am. Chem. Soc.* **2020**, *142*, 9920–9924.
- (36) Ghana, P.; Rump, J.; Schnakenburg, G.; Arz, M. I.; Filippou, A. C. Planar Tetracoordinated Silicon (ptSi): Room-Temperature Stable Compounds Containing Anti-van't Hoff/Le Bel Silicon. *J. Am. Chem. Soc.* **2021**, *143*, 420–432.
- (37) Claes, P.; Ngan, V. T.; Haertelt, M.; Lyon, J. T.; Fielicke, A.; Nguyen, M. T.; Lievens, P.; Janssens, E. The structures of neutral transition metal doped silicon clusters,  $Si_nX$  ( $n = 6–9$ ;  $X = V, Mn$ ). *J. Chem. Phys.* **2013**, *138*, 194301.
- (38) Lu, S. J.; Wang, M. Y.; Wu, L. S.; Wu, Y. F. Modification of geometrical and electronic structures of anionic and neutral silicon clusters by double-doped tantalum atoms. *Mol. Phys.* **2020**, *118*, e1770883.
- (39) Farooq, U.; Naz, S.; Xu, H.; Yang, G. B.; Xu, X. L.; Zheng, W. J. Recent progress in theoretical and experimental studies of metal-doped silicon clusters: Trend among elements of periodic table. *Coord. Chem. Rev.* **2020**, *403*, 213095.
- (40) Schiegerl, L. J.; Karttunen, A. J.; Klein, W. T.; Fassler, E. Silicon clusters with six and seven unsubstituted vertices via a two-step reaction from elemental silicon. *Chemical Science*. **2019**, *10*, 9130–9139.
- (41) Xu, L.; Piao, H.; Liu, Z.; Cui, C.; Yang, D. Sensitized electroluminescence from erbium doped silicon rich oxynitride light emitting devices. *J. Lumin.* **2021**, *235*, 118009.
- (42) Dong, X.; Yang, Z.; Yang, J. Study on the growth behavior and photoelectron spectroscopy of neodymium-doped silicon nanoclusters  $NdSi_n^{0/-}$  ( $n = 8–20$ ) with a double-hybrid density functional theory. *J. Mol. Model.* **2021**, *27*, 1–11.
- (43) Lu, J.; Lu, Q.; Yang, J. Probing the electronic structures and properties of neutral and charged  $FeSi_n(-1,0,+1)$  ( $n = 1–6$ ) clusters using ccCA theory. *J. Mol. Model.* **2020**, *26*, 1–11.
- (44) Pei, W.; Zhou, S.; Bai, Y. Solar Driven  $CO_2$  Hydrogenation on Ti-Doped Silicon Nanocages. *J. Clust. Sci.* **2020**, *31*, 627–635.
- (45) Fan, Y.-W.; Wang, H. Q.; Li, H.-F. Probing the structural and electronic properties of anionic europium-doped silicon clusters by density functional theory and comparison of experimental photoelectron spectroscopy. *Chem. Phys.* **2020**, *538*, 110918.
- (46) Li, C. G.; Gao, J.-H.; Zhang, J. W.-T.; Song, Liu, S.-Q.; Gao, S.-Z.; Ren, B.-Z.; Hu, Y.-F. Structures, stabilities and electronic properties of boron-doped silicon clusters  $B_3Si_n$  ( $n = 1–17$ ) and their anions. *Mol. Phys.* **2019**, *117*, 382–394.
- (47) Zhao, J.; Du, Q.; Zhou, S.; Kumar, V. Endohedrally doped cage clusters. *Chem. Rev.* **2020**, *120*, 9021–9163.
- (48) Truong, N. X.; Jaeger, B. K. A.; Gewinner, S.; Fielicke, A.; Dopfer, O.; Schöllkopf, W. Infrared Spectroscopy and Structures of Boron-Doped Silicon Clusters ( $Si_nB_m$ ,  $n = 3–8$ ,  $m = 1–2$ ). *J. Phys. Chem. C* **2017**, *121*, 9560–9571.
- (49) Truong, N. X.; Savoca, M.; Harding, D. J.; Fielicke, A.; Dopfer, O. Vibrational spectra and structures of  $Si_nC$  clusters ( $n = 3–8$ ). *Phys. Chem. Chem. Phys.* **2015**, *17*, 18961–18970.
- (50) Truong, N. X.; Savoca, M.; Harding, D. J.; Fielicke, A.; Dopfer, O. Vibrational spectra and structures of neutral  $Si_nX$  clusters ( $X = Be, B, C, N, O$ ). *Phys. Chem. Chem. Phys.* **2014**, *16*, 22364–22372.
- (51) Avaltroni, F.; Steinmann, S. N.; Corminboeuf, C. How are small endohedral silicon clusters stabilized? *Phys. Chem. Chem. Phys.* **2012**, *14*, 14842–14849.
- (52) Maneri, A. H.; Singh, C. P.; Kumar, R.; Maibam, A.; Krishnamurty, S. Mapping the Finite-Temperature Behavior of Conformations to Their Potential Energy Barriers: Case Studies on  $Si_6B$  and  $Si_5B$  Clusters. *ACS Omega*. **2022**, *7*, 6167–6173.
- (53) Nazrulla, M. A.; Krishnamurty, S. Stretching the threshold of reversible dynamics in silicon clusters: A case of carbon alloyed  $Si_6$ . *J. Chem. Phys.* **2016**, *145*, 124306.
- (54) Joshi, K.; Maibam, A.; Krishnamurty, S. Finite temperature behaviour of carbon atom-doped silicon clusters: depressed thermal stabilities, coexisting isomers, reversible dynamical pathways and fragmentation channels. *New J. Chem.* **2021**, *45*, 8217–8227.
- (55) Lerner, H. W.; Scholz, S.; Bolte, M.; Wiberg, N.; Nöth, H.; Krossing, I. Synthesis and structures of alkaline-earth metal super-silanides:  $tBu_3SiMX$  and  $tBu_3Si-M-SitBu_3$  ( $M = Be, Mg$ ;  $X = Cl, Br$ ). *Eur. J. Inorg. Chem.* **2003**, *2003*, 666–670.
- (56) Naglav, D.; Tobey, B.; Dzialkowski, K.; Jansen, G.; Wölper, C.; Schulz, S. Insights into molecular beryllium–silicon bonds. *Inorganics* **2017**, *5*, 22.
- (57) Saulys, D. A.; Powell, D. R. Synthesis, experimental/theoretical characterization, and thermolysis chemistry of  $CpBe(SiMe_3)$ , a molecule containing an unprecedented beryllium–silicon bond. *Organometallics* **2003**, *22*, 407–413.
- (58) Liu, X.; Zhang, M.; Yu, S.; et al. Beryllium–beryllium double- $\pi$  bonds in the octahedral cluster of  $Be_2(\mu_2-X)_4$  ( $X = Li, Cu, BeF$ ). *Phys. Chem. Chem. Phys.* **2018**, *20*, 23898–23902.
- (59) Köster, A. M.; Calaminici, P.; Casida, M. E.; Moreno, R. F.; et al. *deMon2k*; *deMon deVelopers*, Cinvestav: Mexico City, Mexico, 2006.



- (60) Becke, D. Density-functional exchange-energy approximation with correct asymptotic behavior. *Phys. Rev. A* **1988**, *38*, 3098–3100.
- (61) Lee, C.; Yang, W.; Parr, R. G. Development of the Colle-Salvetti correlation-energy formula into a functional of the electron density. *Phys. Rev. B* **1988**, *37*, 785–789.
- (62) Köster, M.; Flores-Moreno, R.; Reveles, J. U. Efficient and reliable numerical integration of exchange-correlation energies and potentials. *J. Chem. Phys.* **2004**, *121*, 681–690.
- (63) Perdew, J. P.; Burke, K.; Ernzerhof, M. Generalized gradient approximation made simple. *Phys. Rev. Lett.* **1996**, *77*, 3865–3868.
- (64) Zhao, Y.; Truhlar, D. G. The M06 suite of density functionals for main group thermochemistry, thermochemical kinetics, non-covalent interactions, excited states, and transition elements: Two new functionals and systematic testing of four M06-class functionals and 12 other functionals. *Theor. Chem. Acc.* **2008**, *120*, 215–241.
- (65) Nosé, S. A. Unified formulation of the constant temperature molecular dynamics methods. *J. Chem. Phys.* **1984**, *81*, 511–519.
- (66) Hoover, W. G. Canonical dynamics: equilibrium phase-space distributions. *Phys. Rev. A* **1985**, *31*, 1695–1697.
- (67) Luo, Y.-R. *Comprehensive handbook of chemical bond energies*, 1st ed.; CRC Press: Boca Raton, FL, 2007.
- (68) Zhao, Y.-R.; Bai, T. T.; Jia, L. N.; Xin, W.; Hu, Y. F.; Zheng, X. S.; Hou, S. T. Probing the structural and electronic properties of neutral and anionic lanthanum-doped silicon clusters. *J. Phys. Chem. C* **2019**, *123* (47), 28561–28568.
- (69) Zhao, Y.; Xu, Y.; Chen, P.; Yuan, Y.; Qian, Y.; Li, Q. Structural and electronic properties of medium-sized beryllium doped magnesium BeMg clusters and their anions. *Results Phys.* **2021**, *26*, 104341.